

X-ray Shapes of Distant Clusters: the Connection to Blue Galaxy Fractions

Q. Daniel Wang and Melville P. Ulmer

Dearborn Observatory, Northwestern University
2131 Sheridan Road, Evanston, IL 60208-2900

E-mail: wqd@nwu.edu and ulmer@ossenu.astro.nwu.edu

ABSTRACT

Based on *ROSAT* PSPC pointed observations, we have determined the aggregate X-ray shapes of 10 distant ($z = 0.17 - 0.54$) rich clusters: A2397, A222, A520, A1689, A223B, A1758, A2218, A2111, A2125, and CL0016+16. Four of the clusters have global X-ray ellipticities $\gtrsim 0.2$, as measured on a scale of diameter $\sim 3h_{50}^{-1}$ Mpc. These strongly elongated clusters tend to show substantial amounts of substructure, indicating that they are dynamically young systems. Most interestingly, the global X-ray ellipticities of the clusters correlate well with their blue galaxy fractions; the correlation coefficient is 0.75 with a 90% confidence range of 0.44-0.92. This correlation suggests that blue cluster galaxies originate in the process of cluster formation, and that the blue galaxy proportion of a cluster decreases as the intracluster medium relaxes onto equipotential surfaces.

Subject headings: cosmology: observations — large-scale structure of universe — galaxies: clusters: general — galaxies: evolution — X-rays: general

1. Introduction

By comparing the rest-frame colors of cluster galaxies relative to those of early-type galaxies at the same epoch, Butcher & Oemler (1984; BO84 hereafter) found that the blue galaxy fraction f_b in rich clusters decreases rapidly with time since $z \sim 0.4$. This so-called Butcher & Oemler effect has also been confirmed spectroscopically (Dressler & Gunn 1992 and references therein). While the true nature of the effect remains uncertain (Oemler et al. 1997 and references therein), finding a connection of the blue galaxy proportion to other cluster properties may provide insights into the origin and evolution of blue cluster galaxies.

We here report the detection of a correlation between the f_b values and the global X-ray ellipticities of 10 distant ($z \gtrsim 0.1$) clusters that were optically surveyed by BO84. We first discuss the selection of the clusters, the X-ray observations, and the data reduction (§2), and we then briefly describe both the algorithm used for the X-ray morphological analysis and Monte-Carlo

simulations to assess systematic effects (§3). We present the analysis of the correlation in §4. Since only the projected shapes of the clusters are measured here, we start §5 by acknowledging ambiguities caused by projection effects, and we then consider both the origin and evolution of cluster elongation and how they relate to the Butcher & Oemler effect. Finally in §6, we summarize our results and conclusions. As in BO84 we adopt $H_o = 50 \text{ km s}^{-1} \text{ Mpc}^{-1}$ and $q_o = 0.1$ throughout the paper.

2. X-ray Images

Table 1 lists the salient parameters of both our selected clusters and *ROSAT* PSPC observations (Tümper 1992 and references therein). As a measure of cluster optical richness, the parameter $N_{30\%}$ is between 23 and 155 for these clusters (Table 1), compared to 21 and 94 for Virgo and Coma — two best-known nearby clusters. The only other distant BO84 cluster that was also observed with the PSPC, but is not included in this study, is A777 ($z = 0.226$, $f_b = 0.05 \pm 0.08$, $N_{30\%} = 15$). This cluster is the poorest in the BO84 sample, and its PSPC observation shows little (if any) diffuse emission from the cluster. The observations of A2111 and A520 were obtained by us, while the other seven (both A222 and A223 were covered by the same observation) were retrieved from the *ROSAT* archive (<http://heasarc.gsfc.nasa.gov/>). We constructed X-ray images in the 0.5-2 keV band (PSPC channels: 52-201; Fig. 1) to maximize cluster-to-background contrasts (Wang, Ulmer, & Lavery 1997).

Table 1
Cluster Parameters and X-ray Observations^a

Cluster	z	f_b	$N_{30\%}$	ROSAT No.	Exposure (s)	ellipticity		Position Angle (deg, N-E)	
		(%)				$D = 3 \text{ Mpc}$	$D = 1.5 \text{ Mpc}$	$D = 3 \text{ Mpc}$	$D = 1.5 \text{ Mpc}$
A2397	0.222	1 ± 3	23	wp800344	13152	0.07(0.00-0.15)	0.08(0.00-0.19)	155(117-213)	230(161-276)
CL0016+16	0.541	2 ± 7	65	rp800253	40562	0.07(0.00-0.11)	0.21(0.15-0.27)	61(36-84)	50(42-57)
A222	0.211	6 ± 4	45	rp800048	6780	0.10(0.02-0.26)	0.27(0.17-0.45)	70(41-129)	98(75-113)
A520	0.203	7 ± 7	126	rp800480	4592	0.08(0.00-0.15)	0.17(0.06-0.25)	96(27-159)	11(0.8-31)
A1689	0.175	9 ± 3	124	rp800248	13957	0.16(0.12-0.19)	0.14(0.11-0.17)	183(176-189)	22(16-27)
A1758	0.280	9 ± 4	91	rp800047	13509	0.16(0.10-0.23)	0.42(0.33-0.46)	152(139-169)	123(119-129)
A223B	0.207	10 ± 6	67	rp800048	6780	0.53(0.45-0.58)	0.23(0.10-0.33)	22(17-26)	183(164-212)
A2218	0.171	11 ± 4	114	wp800097	37014	0.24(0.22-0.27)	0.20(0.18-0.23)	96(92-100)	91(86-95)
A2111	0.228	16 ± 3	155	rp800479	7288	0.36(0.27-0.46)	0.39(0.33-0.46)	153(145-160)	145(140-152)
A2125	0.247	19 ± 3	62	rp800511	18352	0.38(0.29-0.48)	0.37(0.27-0.44)	132(124-140)	127(118-135)

^aThe redshift z , the blue galaxy fraction f_b , and the 30% of the total number of cluster members (brighter than $M_v \sim -20$) $N_{30\%}$ are from Butcher & Oemler (1984). Uncertainties in parameter values, as presented in parentheses, are at the 90% confidence level.

We excised from the X-ray images point-like sources detected with signal-to-noise ratios $\gtrsim 3$. The PSPC count distributions of these sources are consistent with the instrument point response function (PSF; $\sim 25''$ FWHM on-axis) at a confidence $\gtrsim 5\%$. The data within the 90% source flux-encircled radius around each source were replaced by randomly generated events of the

intensity interpolated from neighboring pixels. From Monte Carlo simulations (§3), we find that residual source fluxes in the images produce negligible effects on our measurement of global X-ray shapes of the clusters, in comparison to statistical uncertainties.

A few of the images are contaminated by neighboring diffuse X-ray objects. A1758: This cluster has a companion about $8'$ south (the distance between the cluster centroids; Mushotzky 1992). A small portion of this companion, whose redshift is yet unknown, appears in the bottom of the A1758 image. A223B: This cluster image also contains A223A ($z = 0.206$; Sandage, Kristian, & Westphal 1976) and a small section of A222 at the lower right corner. The redshift differences, together with the large projected separations in the sky, indicate that these clusters are not physically interacting with each other. A223A, about $4'$ northeast to A223B, is much fainter in X-rays than A223B. A2125: This cluster is associated with a filamentary feature of low surface brightness diffuse X-ray emission (Wang, Connolly, Brunner 1997), part of which can be seen at the southwestern corner of the image. In order to avoid these extraneous features, we chose a maximum scale of *diameter* $D \sim 3$ Mpc to characterize the global X-ray shapes of the clusters.

3. X-ray Shapes

We characterized the aggregate X-ray shapes of the clusters, using ellipse parameters (centroid, ellipticity ϵ , and position angle). An iterative algorithm for the parameter computation has been detailed by Wang, Ulmer, & Lavery (1997). Here we only outline the procedure. For each cluster, we started an iteration with the calculation of the first and second moments of the source-excised PSPC count distribution within a circular region of diameter D around an assumed cluster centroid. From the moments, we then derived the ellipse parameters, which defined an elliptical region of major axis D for the next run. This iteration went on until all the ellipse parameters converged with relative parameter changes all less than 10^{-3} . In each iteration we subtracted background contributions to the moments. The background level was estimated in an annulus between $10'-16'$ radii from the cluster centroid. We estimated the statistical uncertainties in the final ellipse parameters, using 1000 replications from bootstrapping realizations of the count distribution. The 90% confidence interval of each parameter, for example, represents the 5% and 95% percentiles of the replicated parameter values. Table 1 includes the ellipse parameters measured at two representative scales of $D = 1.5$ Mpc and 3 Mpc.

We also conducted extensive Monte-Carlo simulations to assess systematic uncertainties. Simulated images contain about the same cluster and background counts as observed, and approximate the cluster morphologies with the elliptical β model (e.g., Neumann & Böhringer 1996) of various ellipticities. We randomly added point-like X-ray sources in the simulated images, according to the source luminosity function given by Hasinger et al. (1994). Bright sources were detected and excised as in real X-ray images (§2).

We then applied the above algorithm to these simulated images, which typically reproduced

the model parameters well. But for models of $\epsilon \lesssim 0.05$, the algorithm tended to overestimate the ellipticities. This problem is also present in previous studies of cluster shapes, using similar algorithms (e.g., Carter & Metcalfe 1980; McMillan, Kowalski, & Ulmer 1989; Buote & Canizares 1996). A correction for the problem, which we have not attempted, would only slightly enhance the $\epsilon - f_b$ correlation to be discussed in §4. Furthermore, we find that the effect of residual point-like sources in the X-ray images is negligible in comparison to statistical errors. A superposition of a cluster with an extended source could, however, alter the X-ray morphology of the cluster substantially. But such superpositions with the cores ($D \lesssim 1.5$ Mpc) should be rare occasions for these distant clusters ($\sim 10^{-1}$). A superposition in regions away from cluster cores can easily be recognized, e.g., the A223A/A223B pair. Therefore, these systematic uncertainties should not be important in our study of the *global* X-ray shapes of the clusters.

4. The $\epsilon - f_b$ Correlation

Fig. 2 shows an apparent correlation between ϵ and f_b . Except for A223B, the figure uses the ellipticities as measured on a scale of $D \sim 3$ Mpc (Table 1). Around this scale, the ellipticities typically show little change and is not sensitive to subcomponents occasionally seen in core regions. But for A223B the figure uses the ellipticity measured at $D \sim 1.5$ Mpc to avoid A223A, which is projected at a distance of ~ 1.1 Mpc from A223B (§2.2). We resorted to the bootstrapping method again to quantify the correlation. For each of the 1000 bootstrapping replications of ϵ (§3), we randomly generated a value of f_b , assuming a Normal distribution with the best estimate and 1σ dispersion as listed in Table 1. We made all negative f_b values be zero. Although a measured f_b could be negative due to the statistical uncertainty in the background galaxy subtraction, a negative f_b is physically not real. We calculated the Pearson correlation coefficient for each set of the replications, and then sorted the coefficients from small to large. The median and the 5% and 95% percentiles of the sorted coefficients gave the best estimate and the 90% confidence limits of the coefficient as 0.75(0.44-0.92).

The correlation is less significant on smaller scales. For example, the correlation coefficient is 0.51(0.15-0.77) on the scale of $D \sim 1.5$ Mpc. This weaker correlation is due to the presence of subcomponents in cluster cores. These small-scale subcomponents show little correlation with the global aggregate shapes of the clusters.

5. Discussion

5.1. Projection Effects

While the observed X-ray surface brightness is sensitive only to the emission measure of the hot intracluster medium (ICM), we cannot disentangle the projection effect for individual clusters

with the X-ray images alone. Thus, a circular morphology of a cluster does not necessarily mean a spherical symmetric distribution of the ICM. Projection effects cannot, however, produce an elongated shape of an intrinsically round cluster. The net result of the projection effects is a statistically weaker $\epsilon - f_b$ correlation, and the intrinsic correlation could actually be stronger than the observed. The projection effects should be small, if strongly elongated clusters tend to have triaxial and/or irregular ICM morphologies. Since we are primarily interested in the statistical properties of the clusters, we neglect projection effects in our qualitative discussion below.

5.2. Origin of the Elongated X-ray Morphologies

A2111 and A2125, the two clusters with the largest ellipticities in Fig. 2, are clearly dynamically young systems. A2111 also shows the greatest centroid shift with scale in our cluster sample. A detailed optical and X-ray study of the cluster (Wang, Ulmer, & Lavery 1997) suggests that this cluster is an ongoing coalescence of at least two subclusters. A2125 has a multiple-peak morphology and is associated with a hierarchical superstructure of galaxies, clusters and diffuse hot gas, indicating that the cluster is still at its early stage of formation (Wang, Connolly, Brunner 1997). Therefore, the elongated X-ray morphologies are likely produced during the formation of the clusters.

Theoretically, cluster formation via gravitational attraction naturally results in an elongated mass distribution. Relevant processes include the tidal distortion on the proto-cluster by neighboring objects (Binney & Silk 1979), the triaxial collapse of the density perturbation (Elsenstein & Loeb 1995), and the merger between subunits (e.g., Evrard et al. 1993). When a cluster is just formed, the ICM, following the mass distribution of the dark matter, can thus have a strongly elongated and lumpy morphology, which is manifested by the X-ray emission.

5.3. Evolution of the X-ray Morphologies

As the isotropic pressure tensor of the ICM drives it to lie on equipotential surfaces of a cluster, the aggregate X-ray shape evolves to become smoother and rounder (e.g., Evrard et al. 1993). Hence we argue here that the global X-ray roundness is a cluster age indicator. Nearby rich clusters, more-or-less relaxed, do show significantly rounder X-ray morphologies than the mass distributions (Buote & Canizares 1996). The relaxation should happen on a few sound crossing times in the ICM. The crossing time can be estimated as $t_s \sim (4 \times 10^9 \text{ years})(T_g/3 \times 10^7 \text{ K})^{-1/2}(D/3 \text{ Mpc})$, where the ICM temperature T_g may fall considerably from the core to the outskirts of a cluster, and the scaled value is the characteristic mean temperature of the high ϵ clusters (A2111 — Wang, Ulmer, & Lavery 1997; A2125 — Wang, Connolly, & Brunner 1997). In comparison, the timescale for the cluster to wipe out a subcomponent of a few times hundred kpc across is $\sim 10^9$ years. Such subcomponents presumably represent merging subgroups, whose X-ray emission can be strongly

enhanced by the high pressure in cluster cores. Numerical simulations of hierarchical structure formation do show that the global X-ray shape of a cluster tends to become increasingly round with time (e.g., Evrard et al. 1993; Katz & White 1993; Buote & Tsai 1995). Therefore, the roundness of the global X-ray shape is a measure of the relaxation state of a cluster.

Since the relaxation timescale for the global X-ray shape of a cluster can be comparable to the epoch duration $\sim 9 \times 10^9$ years from $z \sim 0.4$ to $z \sim 0.1$, one might expect to see statistical evidence for the cluster X-ray shape evolution with z . We, therefore, compare our results with the similar X-ray study of five nearby (< 0.1) clusters (Buote & Canizares 1996): A401, A1656 (Coma), A2029, A2199, and A2256. The optical richness of these clusters is comparable to those in Table 1. Buote & Canizares presented in their Table 4 the aggregate X-ray ellipticities measured on various scales for each of the five clusters. We estimate $\epsilon \sim 0.17, 0.14$, and 0.22 on a scale of $D \sim 3$ Mpc for A401, A2029, A2256. For A1656 and A2199, $\epsilon \sim 0.20$ and 0.14 on the largest scales presented $D \sim 1.9$ Mpc and 2.6 Mpc, respectively; the ellipticities at $D \sim 3$ Mpc should be smaller. The errors in these measurements are typically $\lesssim 15\%$. The relatively large ellipticity of A2256 is due to an exceptionally prominent subcomponent of the cluster (e.g., Briel & Henry 1994). In comparison, four out of the ten distant clusters in Table 1 have $\epsilon \gtrsim 0.2$ at $D \sim 3$ Mpc. Thus the evidence for the evolution, if present, is still weak, which may be due to the small number statistics presented here and to the large dispersion in cluster ages at every epoch.

5.4. Implications for the Butcher & Oemler Effect

In contrast, the correlation between the blue galaxy fraction and the global X-ray shape is strong enough to show up in a sample of 10 objects, indicating an intrinsic connection between galaxy evolution and cluster dynamics. This connection is consistent with the notion the Butcher & Oemler effect is due to the transformation of late-type galaxies into early-type ones in clusters formed through hierarchical clustering (Kauffmann 1995; Oemler et al. 1997). In a hierarchical clustering scenario, a typical distant cluster is assembled from smaller units and over a *shorter* period than a nearby cluster of the same mass. Because smaller units tend to contain more gas-rich late-type galaxies, distant clusters are born with larger proportions of such galaxies than nearby ones. Blue galaxies observed in distant clusters are indeed typically gas-rich, starforming, or even starburst spirals/irregulars (e.g., Lavery & Henry 1994; Oemler et al. 1997). Starbursts can be triggered by gas compression, due to both the high ICM pressure and the tidal forces from the mean cluster potential and from frequent encountering cluster members (Henriksen & Byrd 1996; Moore et al. 1996). Such “galaxy harassment” by the cluster environment can also transform late-type blue galaxies to early-type red ones, resulting in the decline of the blue cluster galaxy proportion with time (Oemler et al. 1997). While details about this transformation are still elusive, the presence of the $\epsilon - f_b$ correlation suggests that the transformation process operates on a timescale similar to that of the ICM relaxation from a strongly elongated morphology at the cluster’s birth to a more-or-less round shape.

6. Summary and Conclusion

We have measured the aggregate X-ray shapes of 10 BO84 clusters in the redshift range between $z = 0.17 - 0.54$. Strongly elongated clusters typically show irregular X-ray morphologies (e.g., multiple peaks and centroid shifts), and are probably formed only recently as the coalescences of subunits. Because the ICM tends to relax onto the equipotential surfaces of a cluster, the roundness of the global X-ray shape is a good indicator of the dynamic relaxation state of the ICM.

The ellipticity measured at diameter $D \sim 3$ Mpc of a cluster correlates well with the blue galaxy fraction. This correlation results naturally from the combined action of the cluster formation through hierarchical clustering and the environmental transformation of cluster galaxies from late-types into early-types, if the transformation takes place on a timescale comparable to that of the global ICM relaxation.

This connection of the global X-ray shape of a cluster to both the ICM relaxation state and the blue galaxy proportion, if quantified with improved number statistics, will offer insights into environmental effects on cluster galaxy evolution and will provide a powerful tool for studying distant clusters.

This project is supported by NASA under Grant 5-2717.

REFERENCES

Binney, J. J., & Silk, J. 1979, MNRAS, 188, 273

Briel, U. G., & Henry, J. P. 1994, Nature, 372, 439

Buote, D. A., & Canizares, C. R. 1996, ApJ, 457, 565

Buote, D. A., & Tsai, J. C. 1995, ApJ, 439, 29

Butcher, H., & Oemler, A. 1984, ApJ, 285, 426

Carter, D., & Metcalfe, N. 1980, MNRAS, 191, 325

Dressler, A., & Gunn, J. E. 1992, ApJS, 78, 1

Elsenstein, D. J., & Loeb, A. 1995, ApJ, 439, 520

Evrard, A, Mohr, J. J., Fabricant, D. G., & Geller, M. J. 1993, ApJ, 419, L9

Hasinger, G., et al. 1994, Legacy, 4, 40

Henriksen, M. J., & Byrd, G. 1996, ApJ, 459, 82

Katz, N., & White, S. D. M. 1993, ApJ, 412, 455

Kauffmann, G. 1995, MNRAS, 274, 161

Lavery, R. J., & Henry, J. P. 1994, ApJ, 426, 524

McMillan, S. L. W., Kowalski, M. P., & Ulmer, M. P. 1989, ApJS, 70, 723

Moore, B., Katz, N., Lake, G., Dressler, A., & Oemler, A. 1996, Nature, 379, 61

Mushotzky, R. F. 1992, in Texas/PASCOS meeting: Clusters of Galaxies

Neumann, D. M., & Böhringer, H. 1996, preprint astro-ph/9607063

Oemler, A., Dressler, A., & Butcher, H. R. 1997, ApJ, 474, 561

Sandage, A., Kristian, J., & Westphal, J. A. 1976, ApJ, 205, 688

Trümper, J. 1992, QJRAS, 33, 165

Wang, Q. D., Connolly, A., & Brunner, R. 1997, ApJL, submitted

Wang, Q. D., Ulmer, M., Lavery, R. 1997, MNRAS, in press

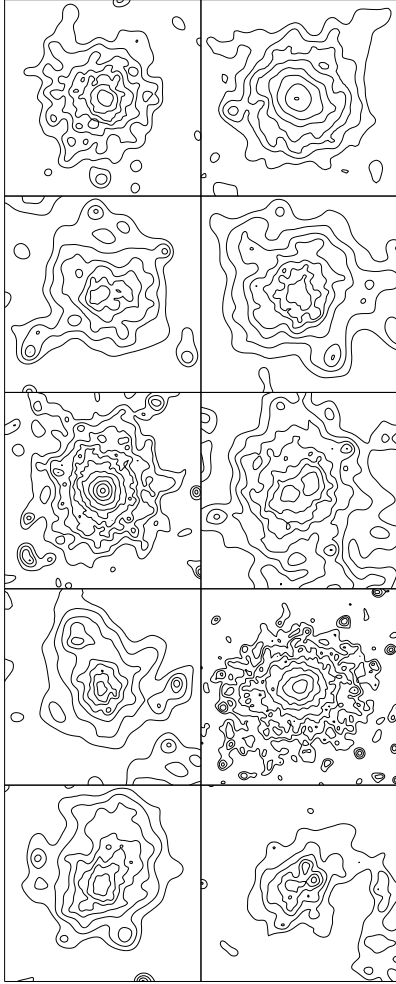


Fig. 1.— 0.5-2 keV band PSPC images of the clusters: A2397, CL0016+16, A222, A520, A1689, A1758, A223B, A2218, A2111, and A2125 (left to right and top to bottom), in order of the f_b values (Table 1). The images all have the same physical scale of 4 Mpc on a side, and have their angular scales of 14.1, 8.2, 14.6, 15.2, 16.8, 12.0, 14.8, 17.1, 13.8 and 13.0 arcmin, respectively. The images, exposure-corrected and background-subtracted and source-excised, are smoothed adaptively with a Gaussian, the size of which is adjusted at each pixel to achieve a count-to-noise ratio of 4. Each contour is a factor of two of its lower level; the lowest contour is at 2.5×10^{-4} counts s^{-1} arcmin $^{-2}$.

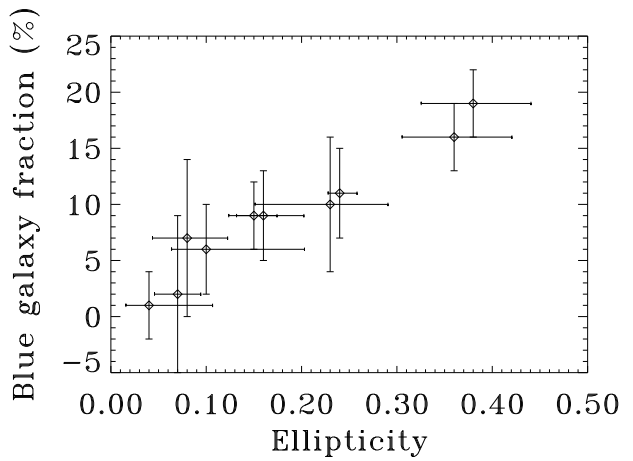


Fig. 2.— Blue galaxy fractions vs. global X-ray ellipticities as measured on a scale of major axis equal to 3 Mpc. The error bars are all at the 1σ level.